



Contents lists available at ScienceDirect

# Colloids and Surfaces A: Physicochemical and Engineering Aspects

journal homepage: [www.elsevier.com/locate/colsurfa](http://www.elsevier.com/locate/colsurfa)

## Evolution of calcite surfaces upon thermal decomposition, characterized by electrokinetics, in-situ XRD, and SEM

Matea Ban<sup>a,b,\*</sup>, Thomas Luxbacher<sup>c,d</sup>, Johannes Lützenkirchen<sup>e</sup>, Alberto Viani<sup>f</sup>,  
Sabrina Bianchi<sup>b,g</sup>, Klaudia Hradil<sup>h</sup>, Andreas Rohatsch<sup>a</sup>, Valter Castelvetro<sup>b,g</sup>

<sup>a</sup> Faculty of Civil Engineering, Research Centre of Engineering Geology, TU Wien, 1040 Vienna, Austria

<sup>b</sup> Department of Chemistry and Industrial Chemistry, University of Pisa, 56124 Pisa, Italy

<sup>c</sup> Anton Paar GmbH, 8054 Graz, Austria

<sup>d</sup> Faculty of Chemistry and Chemical Technology, University of Maribor, 2000 Maribor, Slovenia

<sup>e</sup> Institute for Nuclear Waste Disposal, Karlsruhe Institute of Technology, 76344 Eggenstein-Leopoldshafen, Germany

<sup>f</sup> Institute of Theoretical and Applied Mechanics of the Czech Academy of Sciences, 190 00 Praha, Czech Republic

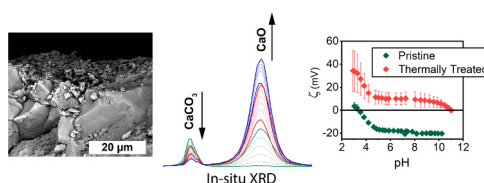
<sup>g</sup> National Interuniversity Consortium of Materials Science and Technology (INSTM), 50121 Florence, Italy

<sup>h</sup> X-Ray Center, TU Wien, 1060 Vienna, Austria

### HIGHLIGHTS

- Thermal decomposition of dense and porous carbonates differs in onset and extent.
- Time-dependend changes of  $\zeta$  for pristine and thermally treated surfaces were studied.
- Contribution of an asymmetric cell configuration to the overall  $\zeta$  was determined.
- $\zeta$ -potential of mixed calcium hydroxide and calcite surfaces was analyzed.

### GRAPHICAL ABSTRACT



### ARTICLE INFO

#### Keywords:

Streaming potential  
Streaming current  
Zeta potential  
Pore conductivity  
Calcium carbonate  
Non-equilibrium

### ABSTRACT

The present study analyses transformation pathways of pristine and thermally treated porous limestone and dense marble surfaces by means of time-resolved streaming current and potential measurements coupled with scanning electron microscopy and in-situ X-ray diffraction. The results reveal that under nonequilibrium conditions the zeta potential ( $\zeta$ ) of natural carbonates may exhibit positive and negative signs and  $\zeta$  drifts in opposite directions. Sample surface roughness influences  $\zeta$  because it contributes to dissolution, as observed particularly in the initial period of time-resolved measurements. Thermal treatment causes a temporary charge reversal from negative to positive. The reactivity of calcium hydroxide on calcite surfaces governs the net electrokinetic potential and isoelectric point ( $\text{IEP}_{\text{pH}}$ ), even at low surface coverage, as cross-validated by in-situ XRD. It was also found that pore conductivity may lead to  $\sim 90\%$  underestimation of  $\zeta$  when assessed by streaming potential. SEM studies revealed micro cracks inducement on marble after thermal treatment, which can result in underestimation of  $\zeta$  up to the same extent as for the porous limestone. When an asymmetric cell configuration involving calcite and polypropylene surfaces is used, the fractional contribution of polypropylene to the  $\text{IEP}_{\text{pH}}$  is 0.3 and to the overall determined  $\zeta$  up to 0.5. Our findings contribute to the understanding of nonequilibrium and time-dependent electrokinetic potential modifications associated with the reactivity of porous surfaces. This study

\* Corresponding author at: Faculty of Civil Engineering, Research Centre of Engineering Geology, TU Wien, 1040 Vienna, Austria.

E-mail address: [matea.ban@tuwien.ac.at](mailto:matea.ban@tuwien.ac.at) (M. Ban).

<https://doi.org/10.1016/j.colsurfa.2021.126761>

Received 8 December 2020; Received in revised form 13 April 2021; Accepted 27 April 2021

Available online 6 May 2021

0927-7757/© 2021 The Author(s). Published by Elsevier B.V. This is an open access article under the CC BY license (<http://creativecommons.org/licenses/by/4.0/>).

highlights the effectiveness of the streaming potential technique for monitoring such changes further supported by the use of ancillary techniques to analyze the extend of chemo-mineralogical and physical alterations.

## 1. Introduction

Surface reactions at mineral-water interfaces govern various processes, including sorption, redox processes, weathering, and other phenomena in many environmental and industrial aspects [1,2]. These processes occur under nonequilibrium conditions, and the heterogeneous nature of the surfaces makes their molecular-level origin difficult to study and understand. Accordingly, the dynamic structure of calcite-water interfaces and the role of ions in their hydrodynamic environments are still largely unresolved [3]. As an example, the electrokinetic charge of calcite remains the subject of ongoing debate, and particularly so with reference to the differing zeta-potential ( $\zeta$ ) behaviors observed by different authors, even when adopting comparable experimental conditions [4]. Despite these discrepancies, the electrokinetic potential of a sample is widely accepted to depend on the initial state of its surface and the composition of the contacting aqueous electrolyte [5,6]. When a solid comes into contact with an aqueous electrolyte and its surface groups react and/or exchange with water and ionic species in the solution, spontaneous surface charge development results. This first adsorbed layer, the immobile layer, contains ions that are tightly bound to the surface and is referred to as the Stern layer. The ions that neutralize the residual excess surface charge beyond the Stern layer are mobile ions and are considered to belong to the diffuse layer. The combination of Stern and diffuse layers are commonly referred to as the electrical double layer (EDL). The electrokinetic potential, i.e.  $\zeta$ , is an experimentally accessible physical parameter that allows characterization of the electrokinetic charge, and it is generally interpreted as the potential at the slipping plane, or shear plane, the exact location of which is the subject of ongoing research, but is expected to be somewhere near the diffuse layer plane (i.e., outer Helmholtz plane) of the standard EDL model.

By moving the electrolyte in a microchannel along the surface under study, the excess charge of the diffuse layer will be dragged along, giving rise to the streaming current. Both electrokinetic phenomena, streaming current and streaming potential, can be measured. According to a recent study [7] in which flat polymer surfaces of differing roughness and textures were investigated, streaming potential data should not be interpreted based solely on absolute  $\zeta$  readings, but rather on trends and plateaus in pH- and concentration-dependent data. Information regarding the electrokinetic potentials of macroscopic calcites with different roughness is scarce, especially for systems under nonequilibrium, i.e. highly reactive, conditions. In one such study, in a different context, Elimelech et al. [8] demonstrated that, in the initial deposition of colloidal particles in heterogeneous porous media, the controlling factor of the kinetics is the degree of chemical heterogeneity (i.e. spatially variable surface reactivity). The term surface reactivity in the context of calcite refers to reactions at the mineral surface, which determine its stability in a given environment or its resistance towards dissolution, while chemical heterogeneity in natural mineral contexts denotes different chemical compounds, including organic matter, trace elements or different phases, among others.

Even more demanding than the study of the electrokinetic potential of calcites is the investigation of calcite charge alterations or time-dependent transformations, as is expected for mixed calcium hydroxide and calcite interfaces in contact with aqueous solutions. Kosmulski [9] pointed out that, due to the solubility of calcium hydroxide and its reactivity towards carbon dioxide, the results reported in the scientific literature for mixed systems may be largely unreliable. Moreover, the actual degree of hydroxylation/hydroxyl coverage is unknown and changes dynamically. However, such systems are responsible for key phenomena in many areas of research and applications. For instance,

knowledge of in-situ reaction pathways could enhance our mechanistic understanding of the coagulation of cement particles [10], carbon dioxide sequestration, and waste carbonation reactions [11], as well as other industrial applications in which basic calcium oxide surfaces are involved [12]. Furthermore, studies on thermal treatment of stone and mineral materials are relevant in order to understand the effect of fire damage on materials used for civil and building structures [13–15] or in concrete technology [16], among others. Although physical changes of stones caused by thermal treatment are well-studied phenomena [17–19], gaps exist concerning research on chemo-mineralogical alterations, especially regarding transition temperatures and the extents of transformation as well as subsequent influences on the surface when the stones are again exposed to the environment and thus in contact with an aqueous electrolyte. In the aforementioned cases the reactions and interactions at interfaces are difficult to follow experimentally. However, as a recent study demonstrated [20], the observation of electrokinetic phenomena can be employed to track in-situ transformations.

In this study, we systematically modified the surface chemistry of metamorphic and sedimentary calcium carbonates by thermal treatment to induce partial phase and chemical transformations. We then determined the electrokinetic potentials of the resulting samples with the aim of improving our understanding of the role of phase transformations and modified (or newly created) porosity and reactivity. It should be noted that electrokinetic potential is investigated in this study and cannot be supplemented by titrable surface charge, which would yield additional insight in the interfacial charge, because it is difficult, if not impossible, to determine for calcite and calcium-hydroxides. Besides streaming current and potential measurements we used in-situ X-ray diffraction (XRD) and scanning electron microscopy (SEM) as ancillary techniques to explore in more detail the involved surface phenomena.

The results obtained contribute to our understanding of solid calcite and mixed calcite and calcium-hydroxide surface reactivity in dynamic environments and provide knowledge for applications where time-resolved reaction pathways are of concern. Furthermore, given the large variability in the results concerning both the magnitude and even polarity of the electrokinetic potential for calcite previously reported in the literature, the characterization strategy described here may also contribute to a more accurate determination of the electrokinetic potential for porous macroscopic, flat materials by considering nonequilibrium and time-dependent changes, including the effects of pore conductivity and reactivity.

## 2. Experimental section

### 2.1. Materials

Two natural carbonate stones, Apuan Marble (AM), often also referred to as Carrara Marble, quarried from the Apuan Alps in Tuscany, Italy, and Lumaquela de Ajarte (LdA), quarried from Ajarte Trevino, Spain, were provided by local quarrying companies. AM has a dense, fine-crystalline metamorphic structure mainly consisting of calcite (~99 wt%), and it is therefore often classified as a monomineralic rock (Fig. 1a). Traces of dolomite and quartz are frequently found in AM, but typically amount to less than 1 wt%. The grains have an average size of 0.1 mm and the grain boundaries make up a large volume fraction of the bulk structure. This lithotype is known for its strength, which is related to its low Hg-open porosity of < 0.7%. LdA is a biogeneous sedimentary lithotype classified as a poorly washed biomicrite (fossil fragments embedded in a matrix derived from calcite mud) to microsparite (sparry calcite cement with readily discernible faces) [21], a so-called wackestone [22], consisting of shell fragments embedded in a carbonate

matrix composed of recrystallized fossil components, mainly foraminifera and echinacea (Fig. 1b). Due to recrystallization, no clear distinction between the inclusion and the cementing minerals is possible, except for some larger biogenic fragments with sizes up to a few millimeters. LdA is both structurally and chemically more heterogeneous than AM. It is composed of  $\sim 96$  wt% calcite and  $\sim 2$  wt% quartz with smaller contributions from elements such as aluminum, magnesium, potassium, and iron, among others. A high amount of small intercrystalline pores and larger calcitic sparite crystals can be observed by thin-section optical microscopy. This limestone has a relatively high Hg-open porosity of  $\sim 24\%$ . Chemical analysis as determined by XRF and porometric properties are available as [Supplementary Data \(Table S1 and S2\)](#).

## 2.2. Calcination

Freshly cut  $50 \times 50 \times 25$  mm<sup>3</sup> specimens of the natural carbonates were studied in their pristine (untreated) and thermally treated conditions. Thermal treatment was performed in an electrically heated Thermo Scientific Heraeus K 114 furnace with a 3.5 L internal volume. The specimens were exposed to three subsequent cycles of thermal treatment consisting of a heating ramp at  $40$  °C min<sup>-1</sup> followed by a 1 h isothermal step at  $600$  °C, and rapid cooling to room temperature before restarting the cycle. The duration of the isothermal step and the heating rate were chosen based on the results of preliminary experiments aimed at avoiding macroscopic failure of the samples (i.e., continuous cracks passing through the specimen). The goal of the cycling treatment was to achieve surface-limited phase transformation, whereby the specimens maintain their outer macroscopic shape and thus allow comparative measurements of  $\zeta$ . The reversibility of chemical surface modifications under ambient storage conditions (in a desiccator open to atmospheric H<sub>2</sub>O and CO<sub>2</sub> at room temperature) allowed time-dependent monitoring of  $\zeta$ . The samples are labeled according to their preparation (pristine and aged) and storage prior to the zeta potential analysis, i.e., Aged<sub>1.5</sub>, Aged<sub>24</sub> and Aged<sub>365</sub> corresponding to storage after thermal treatment for 1.5 h, 24 h and 365 days, respectively.

In order to preserve the morphologies of the altered surfaces for the purpose of SEM studies and to obtain well-contrasted grayscale images from the backscattering detector, which highlight chemo-mineralogical changes, the freshly thermally treated specimens were coated with a nanosilica suspension to consolidate the newly generated morphological features. The silica sol (NC-12C, Colorobbia S.p.A., Sovigliana-Vinci, Italy) was applied five days after the thermal treatment. The silica

suspension comprised  $15 \pm 2$  wt% particles approx. 35 nm in size, in a water-ethanol mixture.

## 2.3. Characterization

### 2.3.1. Physical and chemo-mineralogical characterizations

SEM with energy dispersive X-ray spectroscopy (EDX) was used to qualitatively assess larger surface areas, corresponding more closely to the dimensions of the streaming channel for  $\zeta$ -potential analysis. Size and shape of newly formed phases as well as changes in microstructure were investigated with a QUANTA FEG 450 instrument (FEI-Thermo Fisher Scientific, Inc.). The samples were mounted on aluminum stubs, coated with a 5-nm thick gold film prior to analysis, and observed at 20 kV accelerating voltage in backscatter and secondary electron mode.

Observations for thin sections were conducted with a petrographic microscope (Olympus BX41). The samples were embedded with the resin-hardener system XW 396 / XW 397 (Huntsman Corporation, Salt Lake City UT, USA) in a 10:3 wt ratio and cured overnight at  $40$  °C. Before mixing resin and hardener, 1.3 g Fluorol 008 or EpoDye (Struers Inc., Cleveland OH, USA) was added to 100 g of XW 396. The thin sections were polished to approx. 30  $\mu$ m thickness and analyzed in cross-polarized-, plain polarized- and under UV-light. The characterization under different light helps to detect crystallographic orientations, textural differences or display porosity and cracks.

Additionally, porometric properties, including the total pore surface, average pore size, and open Hg-porosity, were determined using the Porotec Pascal 140/440 porosimeter (Thermo Electron Corporation, former Thermo Fisher Scientific).

Sound speed propagation of longitudinal ultrasonic waves was measured according to EN 14579 [23]. For the test an electrical pulse generator (CONOSONIC C2-GS), a pair of transducers (UP-DW) and an amplifier (VV 41) developed by Geotron-Elektronik (Pirna, Germany) were used. An average of 10 prisms ( $1 \times 1 \times 4$  cm) were tested on a rubber support and a coupling medium made out of clay was used. The frequency amounted to 80 kHz and the amplitude was adjusted according to sample damping.

Surface color measurements were carried out with a ColorLite sph850 spectrophotometer following the standard EN 15886 [24]. These measurements involve the International Commission on Illumination CIE L\*, a\*, b\* color parameters. A D65 illuminant at  $10^\circ$  standard observer with a reflectance spectrum in the range of 400–700 nm was used. An average of three measurements each of (L\*), (a\*), and (b\*) obtained at the same spot of the calcite surface was used to obtain the

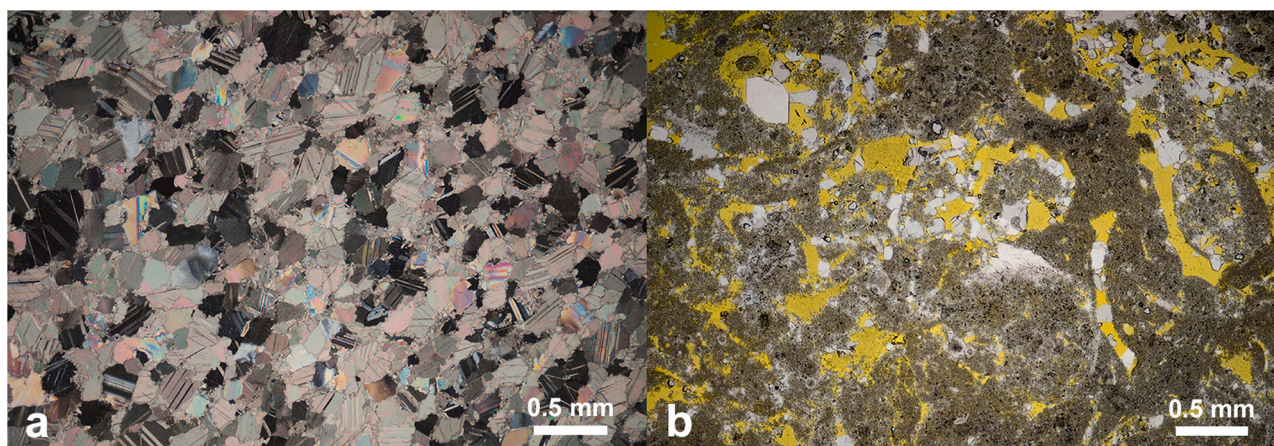


**Fig. 1.** Micrographs showing the fabric of the studied stones as seen in thin sections under the optical microscope. a) Dense, fine-crystalline structure of Apuan Marble under cross-polarized light. The colors represent different crystal orientations. b) Porous, biocalcarene Lumaquela de Ajarte under plane-polarized light. Shell fragments embedded in a matrix composed of recrystallized fossils are visible. The yellow-resin-impregnated thin section demonstrates the porosity of Lumaquela de Ajarte, which is virtually absent in Apuan Marble. (For interpretation of the references to colour in this figure legend, the reader is referred to the web version of this article.)

total color difference ( $\Delta E^*$ ) between pristine (p) and thermally treated (tt) samples using the following equation:

$$\Delta E_{tt,p}^* = \left[ (L_{tt}^* - L_p^*)^2 + (a_{tt}^* - a_p^*)^2 + (b_{tt}^* - b_p^*)^2 \right]^{0.5} \quad (1)$$

Here,  $\Delta L^*$  ( $= L_{tt}^* - L_p^*$ ) corresponds to the lightness difference, ( $\Delta a^*$ ) to the red/green difference, and ( $\Delta b^*$ ) to the yellow/blue difference of the tested stone specimens.  $\Delta E^*$  describes the metric difference or distance between two colors before and after thermal treatment.

Nonambient or in-situ XRD diffractograms were recorded using a PANalytical XPert MPD Pro powder diffractometer (PANalytical B.V., The Netherlands) equipped with a XCelerator detector and working in Bragg-Brentano  $\theta$ - $\theta$  geometry. A partly focusing mirror was used to select the  $\text{CuK}\alpha_{1/2}$  characteristic lines ( $\lambda_{\alpha 1} = 1.54060 \text{ \AA}$ ,  $\lambda_{\alpha 2} = 1.54443 \text{ \AA}$ ) for the experiment. A high-temperature furnace (Anton Paar HTK 1200 N), operating in air under ambient pressure, allowed controlled thermal treatment on disk-shaped stone specimens 18 mm in diameter and  $\sim 2.5 \text{ mm}$  thick. Diffractograms were recorded in-situ during the programmed temperature steps and allow direct observation of phase evolution with temperature. For each temperature step, data was continuously collected in the  $2\theta$  range  $15$ – $90^\circ$  at a speed of  $0.01^\circ \Delta 2\theta/\text{s}$ . Subsequently, the data were analyzed by the HighScore Plus software package [25] using the Powder Diffraction File (PDF4+ [26,27]; International Centre for Diffraction Data, Philadelphia, USA). Rietveld refinement was performed with TOPAS 4.2 [28] (Bruker-AXS) for quantitative analysis of the phases. Essentially, the Rietveld method [29] involves a full-profile fitting procedure, in which the difference between the experimental XRD diffraction profile and the calculated one, according to the information on structure models of each crystalline phase, is minimized through a least-squares procedure. The samples were first studied at room temperature and at selected points during the heating steps up to  $600^\circ \text{C}$  ( $40^\circ \text{C min}^{-1}$  heating ramp) simulating the calcination conditions used earlier. Six subsequent XRD diffraction patterns were collected under isothermal conditions by pausing the heating ramp for 10 min at  $100^\circ \text{C}$ ,  $200^\circ \text{C}$ ,  $300^\circ \text{C}$ ,  $400^\circ \text{C}$ , and  $500^\circ \text{C}$ . At  $600^\circ \text{C}$ , constant temperature for 60 min was imposed, corresponding to six separate XRD data sets collected at this temperature. After thermal treatment, the samples were let to cool down to  $35^\circ \text{C}$  while exposed to room temperature. This heating/cooling cycle was repeated three times to generate sufficient change on the surface layers. All three cycles were recorded by in-situ XRD.

### 2.3.2. Experimental setup for streaming current and potential measurements

Streaming current and potential measurements were performed with a SurPASS™ Electrokinetic Analyzer (Anton Paar GmbH, Austria) using

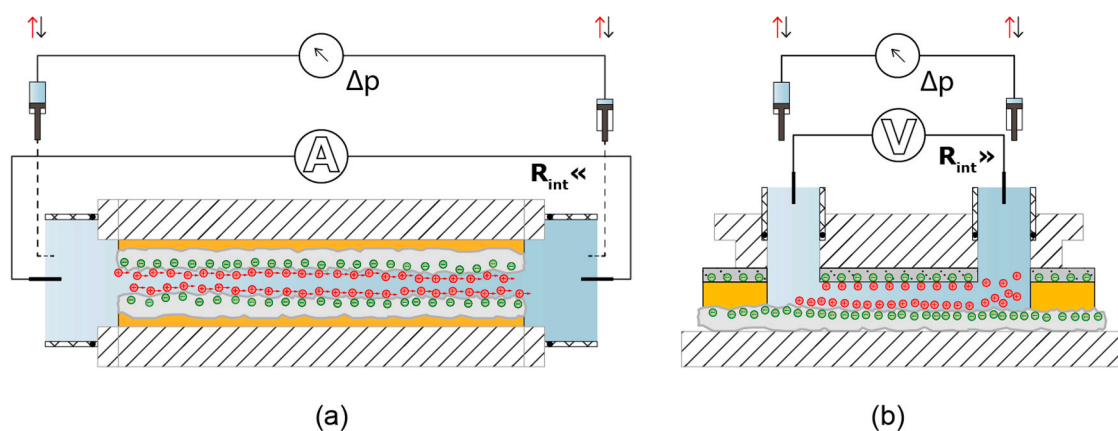
a custom-made clamping cell (CC) with an asymmetric configuration and an adjustable gap cell (AGC) with a symmetric configuration (Scheme 1).

In the CC, the two flat walls of the slit through which the electrolyte solution flows consist of a polypropylene (PP) support serving as a reference surface with holes for liquid inlet/outlet as well as a flat target surface (here a given carbonate sample under investigation). Note that the asymmetric configuration of the streaming channel implies a mixed  $\zeta$  caused by the carbonate and the reference PP surface. The streaming channel, which is  $12.5 \text{ mm}$  in length and  $6 \text{ mm}$  in width, has a gap height of  $< 140 \mu\text{m}$  as fixed by a spacer.

The AGC consists of two flat thin slices of the target carbonate specimen placed opposite each other, creating a channel  $20 \text{ mm}$  in length and  $10 \text{ mm}$  in width with a gap height that can be adjusted mechanically with a precision screw. By allowing the electrolyte solution to flow through the channel, true  $\zeta$  of the material forming the channel walls can be determined as  $\zeta\text{-True}(I_{\text{str}})$  for streaming current or  $\zeta\text{-True}(U_{\text{str}})$  for streaming potential measurements.

Tests performed with the CC configuration comprised pH-dependent electrokinetic measurements performed on pristine, Aged<sub>24</sub>, and Aged<sub>365</sub> surfaces using a  $10^{-3} \text{ M}$  aqueous KCl solution (Carlo Erba Reagents) in milli-Q® water as the background electrolyte. The electrolyte solution was purged with  $\text{N}_2$  throughout the measurements to prevent  $\text{CO}_2$  dissolution. The pH was adjusted in the pH range from 3 to 11 with either  $0.05 \text{ M HCl}$  or  $0.05 \text{ M NaOH}$  (Sigma-Aldrich Chemie GmbH) using the automatic dosing unit of the SurPASS apparatus. Starting pH values were between 5.5 and 6.5. The asymmetric configuration of the CC was generally preferred for studies of surface modification and reactivity because of rapid and precise sample mounting. All measurements were performed at least in duplicate for the pristine and thermally treated calcite. The result reported for each measurement at the given experimental conditions (pH, specimen condition) is the average of four consecutive measurements for which the standard deviation is provided. Before each measurement, the surface of the pristine carbonate was cleaned with pressurized argon to remove any particulate matter. Then the sample was mounted in the measuring cell and rinsed with the probing electrolyte solution for approx. 5 min. This was necessary for proper wetting of the electrodes and to establish laminar flow conditions and contact between the solution and natural carbonate to ensure repeatability of the experimental results.

Continuous time-resolved experiments were also performed using both CC and AGC configurations. AGC experiments comprised long-term, alternating streaming current and streaming potential measurements on pristine calcites. The more accurate AGC setup is difficult to be used for thermally treated calcites owing to (i) the challenging fabrication of the  $< 2 \text{ mm}$  thick, precisely cut stone slices required for the



**Scheme 1.** Schematics of a) the adjustable gap cell (AGC) configuration and b) the clamping cell (CC) with an asymmetric configuration for  $\zeta$  analysis of flat macroscopic surfaces and the generation of either streaming current with a low resistance path or streaming potential with a high resistance path. The dimensions are not to scale.

AGC, resulting in nearly systematic breakdown of the brittle carbonates; (ii) the macroscopic cracks caused by thermal treatment through differential stresses within the small samples; and (iii) the time-consuming adjustment of gap height and flow rate to ensure suitable conditions for flow in the AGC, which causes inevitable, substantial reactions with the surfaces before reliable data could be collected. Long-term experiments performed with the CC configuration included alternating streaming current and potential measurements on thermally treated calcites, labeled as Aged<sub>1.5</sub>. With these specimens, long-term monitoring was possible for a more reactive state, i.e., 1.5 h after the thermal treatment. It should be noted that we intentionally omitted the use of samples in such a reactive state for all tests because re-carbonation induced gluing of the specimens to the sample holder. In addition, the AGC configuration allowed to determine the fractional contribution of the reference PP surface to the overall measured  $\zeta$ .

### 2.3.3. Calculation of $\zeta$ , corrections for permeability and pore conductivity and fractional contribution of the reference surface to the measured $\zeta$

The value of  $\zeta$  is evaluated from the streaming potential or streaming current that arise due to the electrolyte flow generated by an applied pressure gradient tangential to the surface of the material under study. Evaluation of  $\zeta$  is usually done via the well-known Helmholtz–Smoluchowski equation for streaming current:

$$\zeta(I_{Str}) = \frac{dI_{Str}}{d\Delta p} \frac{\eta}{\epsilon \epsilon_0} \frac{L}{A}; \quad (2)$$

where  $\zeta(I_{Str})$  represents the  $\zeta$ -potential derived from streaming current measurements,  $\left(\frac{dI_{Str}}{d\Delta p}\right)$  is the streaming current coupling coefficient experimentally obtained from the slope of the linear fit of streaming current [A] to pressure difference ( $\Delta p$ ) ramp [Pa],  $\eta$  is the dynamic viscosity of the electrolyte [Pa s], and  $\epsilon$  and  $\epsilon_0$  are the dielectric constant of the electrolyte solution and the vacuum permittivity [ $8.854 \times 10^{-12}$  F m<sup>-1</sup>], respectively.

Since Eq. (2) applies under laminar flow conditions, and the flow regime is related to the geometry of the streaming channel and the flow rate, the factors affecting such properties must be accounted for. For a microchannel of length  $L$  [m] and rectangular cross-sectional area  $A$  [m<sup>2</sup>] given by channel width  $W$  and height  $H$ , from the Hagen-Poiseuille relation and according to the approximation of Bruus [30], the volume flow rate  $\dot{V}$  [m<sup>3</sup>s<sup>-1</sup>] is given by Eq. (3):

$$\dot{V} = \frac{dV}{dt} = \frac{H^3 W}{12\eta L} \Delta p [1 - 0.630 HW^{-1}]. \quad (3)$$

When  $H < W$ , i.e.,  $HW^{-1} \rightarrow 0$ , the last term  $[1 - 0.630 HW^{-1}] \approx 1$  and the gap height is obtained:

$$H = \left(12\eta \frac{L}{W} \frac{\dot{V}}{\Delta p}\right)^{1/3}; \quad (4)$$

where the gap height of the microchannel is determined by the volume flow rate versus pressure difference and the linear dependence of  $\dot{V} \propto \Delta p$  assumes laminar flow conditions. To account for the actual dimensions of the flow channel, which becomes necessary when different measuring cells are used, the following relationship applies:

$$\frac{\zeta_{I_{Str}}^{app}}{\zeta_{I_{Str}}^{corr}} = \frac{L}{A}; \quad (5)$$

which uses the apparent or measured values ( $\zeta_{I_{Str}}^{app}$ ), as reported by the instrument software, over the corrected values ( $\zeta_{I_{Str}}^{corr}$ ), as given by the custom-made cell. By rearranging, the geometrical corrections can be accounted for through Eq. (6):

$$\zeta_{I_{Str}}^{corr} = \frac{L^1}{L} \frac{W}{W^1} \frac{H}{H^1} \zeta_{I_{Str}}^{app}. \quad (6)$$

The gap height of the channel is calculated from the ratio between volume flow rate and pressure difference, but since a transition from laminar to turbulent flow may occur in the case of highly porous carbonates, a correction for potential nonlinear dependency might be necessary (see Fig. S1). Taking the corrected term ( $H^1$ ) over the apparent gap height ( $H$ ), Eq. (7) is obtained:

$$H^1 = \left(\frac{k^1}{k} \frac{L^1}{L} \frac{W}{W^1}\right)^{1/3} H; \quad (7)$$

where ( $k$ ) and ( $k^1$ ) equal  $\left(\frac{\dot{V}}{\Delta p}\right)$  as linear and polynomial fits, respectively.

Linear regression of nonlinear dependency would underestimate the gap height. The slope of a second-order polynomial fit at  $\Delta p \rightarrow 0$  Pa describes the permeability of the flow channel more reliably. Therefore, by inserting Eq. (7) into Eq. (6), the geometrical correction can be introduced as follows:

$$\zeta_{I_{Str}}^{corr} = \left(\frac{k}{k^1}\right)^{1/3} \left(\frac{L^1}{L} \frac{W}{W^1}\right)^{2/3} \zeta_{I_{Str}}^{app}, \quad (8)$$

where ( $\zeta_{I_{Str}}^{corr}$ ) estimates the corrected  $\zeta$ -potential of the studied porous carbonate surfaces.

An additional approximation of Eq. (2) regards the related electrokinetic phenomenon, the streaming potential given by Eq. (9):

$$\zeta(U_{Str}) = \frac{dU_{Str}}{d\Delta p} \frac{\eta}{\epsilon \epsilon_0} \kappa_B; \quad (9)$$

where  $\left(\frac{dU_{Str}}{d\Delta p}\right)$  denotes to the streaming potential coupling coefficient [VPa<sup>-1</sup>] and  $\kappa_B$  the conductivity of the bulk electrolyte solution [S m<sup>-1</sup>]. The latter value is an additional parameter that needs to be measured and as such it introduces additional errors when intrinsic  $\zeta$  values need to be obtained. This is why Eq. (2) is more convenient for calculating  $\zeta$  when the channel geometry is known.

Since even sparingly soluble minerals like calcium carbonate dissociate in water, yielding a weak electrolyte solution, dissolution phenomena at the material surface release ions, which contribute to the conductivity inside the streaming channel (and also to the conductivity of the bulk electrolyte solution). As the resulting increased conductivity would lead to an underestimation in the calculation of  $\zeta$ , corrections are necessary. The farther the material under study is from equilibrium conditions, the larger is the possible deviation from the unperturbed model. At this point, the difference between surface conductivity and the ionic or pore conductivity needs to be emphasized. Both properties will underestimate  $\zeta$  obtained through streaming potential measurements, but they refer to different phenomena. To analyze if surface conductivity effects can be neglected in the case of flat surfaces, the channel heights are varied in respect to the liquid bulk conductivity [31,32]. As in the CC configuration the gap height is fixed and the calcite surfaces are rough, the effect of pore conductivity will dominate and is accounted for through measurements of the electric resistance  $R$  along the streaming channel by using the ratio of streaming potential and streaming current:

$$\frac{U_{Str}}{I_{Str}} = R. \quad (10)$$

This approach represents a simplified case and neglects effects of surface conductivity on the determined  $\zeta$ -( $U_{Str}$ ), which diminish at conditions of  $\geq 1$  mM KCl and gap heights  $> 50$   $\mu$ m as employed in the present work. Surface conductivity was accounted for in various experimental settings where the electrolyte flows through porous media [33,34]. To account for the effect of ionic or pore conductivity for flat

solid surfaces, Eq. (11) is obtained:

$$\frac{\zeta_{U_{Str}}^{app}}{\zeta_{U_{Str}}^{corr}} = \frac{\kappa_B}{\kappa_B^1} \text{ where } \kappa_B^1 = \left( \frac{1}{R} \frac{L}{A} \right). \quad (11)$$

$\kappa_B^1$  corresponds to the measured electrical conductivity inside the streaming channel as a function of the channel geometry. By solving for correct  $\zeta$  values, we obtain Eq. (12):

$$\zeta_{U_{Str}}^{corr} = \frac{1}{\kappa_B} \kappa_B^1 \zeta_{U_{Str}}^{app}. \quad (12)$$

The use of streaming potential relies on the substitution of the streaming current using Ohm's law ( $I = U/R$ , where  $R$  [Ohm] is the electrical or cell resistance inside the streaming channel). However, Ohm's law is disobeyed because of the local excess concentration of ions that results in a higher electrical conductivity when compared to the conductivity of the bulk electrolyte solution. This difference can be used to analyze the reactivity of different surfaces and thus, by using Eq. (12), and with the previously introduced corrections for the nonlinear dependency conditions and for channel geometry, Eq. (13) is derived:

$$\zeta_{U_{Str}}^{corr} = \left( \frac{1}{\kappa_B} \right) \left( \frac{1}{R} \frac{L}{A} \right) \left( \frac{k}{k^1} \right)^{1/3} \left( \frac{L^1}{L} \frac{W}{W^1} \right)^{2/3} \zeta_{U_{Str}}^{app}. \quad (13)$$

Fairbrother and Mastin [35] assumed that surface conductivity is suppressed when the conductivity of the electrolyte is high. However, when altering the surface, the conductivity of the contacting electrolyte solution may be modified, particularly for porous surfaces. This effect of pore conductivity and related changes in the streaming channel may become a key issue for porous carbonates, which ultimately requires the corrections introduced in Eq. (13). Since the measurements in the present work were carried out under nonequilibrium conditions, the ionic conductivity of the sample may be used as an indicator of surface reactivity. In fact, the observed changes caused by material contribution (dissolution and ion accumulation) to the overall conductivity can be used to study porosity alterations and reactivity in dynamic environments by:

$$\kappa_B^1 - \kappa_B \approx \text{poreconductivity}. \quad (14)$$

It should be noted that the absolute values of pore conductivity depend on both cell resistance and bulk conductivity. Therefore, they can only be compared for same cell configurations and sample conditions.

If the CC is used, the fractional contribution of the reference PP surface to the overall determined  $\zeta$  needs to be considered. Walker et al. [36] assumed equal contributions from their reference surface and different sample surfaces. As streaming potential techniques directly related to the average  $\zeta_{Avg}$ , knowledge of either  $\zeta_{Ref}$  of the reference surface or  $\zeta_{Test}$  of the tested material is required to achieve a complete information on the system according to the following relation:

$$\zeta_{Test} = 2\zeta_{Avg} - \zeta_{Ref}. \quad (15)$$

In an earlier study Elimelech et al. [8] used a linear combination of the  $\zeta$  values of two mixed materials:

$$\zeta_{Avg} = \lambda\zeta_1 + (1-\lambda)\zeta_2; \quad (16)$$

where  $\lambda$  and  $1-\lambda$  are the fractional total surface areas of the two materials characterized by different  $\zeta$  values,  $\zeta_1$  and  $\zeta_2$ . Eq. (15) can be used only in cases where  $\lambda = 0.5$ ; on the other hand, if all terms of Eq. (15) can be measured, the value of  $\lambda$  can be obtained as:

$$\lambda = \frac{\zeta_{Avg} - \zeta_2}{\zeta_1 - \zeta_2}. \quad (17)$$

### 3. Results and discussion

#### 3.1. Analysis of textural changes after thermal treatment

The textural (or rock microstructural) evolution after thermal treatment was investigated by quantifying surface color changes, the formation of microcracks, and the development of new phases on the surface of the carbonates, as observed by polarized light- and scanning electron microscopy. Upon thermal treatment, AM samples turn opaque and dull due to phase transformation and changes caused by the induced microcracks. The surface of AM becomes whiter while LdA undergoes a darkening of the bulk fabric after thermal treatment (see Table 1). The change in LdA's color after thermal treatment ranges from reddish to greyish and it is caused by changes of iron-oxy-hydroxide and iron-oxide or similar iron-bearing minerals present in trace amounts in its fabric. Such color change is controlled by mineralogical alterations also affecting the surface chemistry. Moreover, immediately after the thermal treatment a formation of a whitish surface layer on both carbonates was observed, as a result of quick re-carbonation of the CaO surface layer generated by the thermal treatment and the presence of some reactive calcium hydroxide residues (as can be assessed by a 0.1% phenolphthalein indicator solution).

As the studied stones formed under different conditions, their fabric differs (see Fig. 2a–d), which normally implies that their response to thermal treatment will vary. Crack development is the result of thermomechanical stresses caused by several contributions. The most important one is the strong anisotropy of the thermal expansion coefficient of calcite, which is positive along its c-axis and negative perpendicular to it [37]. For AM, the microcracks are more pronounced, owing to its dense structure. The cracks were found to be of both inter- and trans-granular nature, resulting in increased porosity and newly generated exposed surfaces (Fig. 2e). Such severe changes on AM are also displayed by the porometric data (Table 2), showing a noticeable increase in average pore size and total porosity after thermal treatment. Conversely, the porous LdA is more effective in accommodating stresses due to the pore space available for thermal expansion, preventing strain accumulation at interfaces between neighboring minerals, so that the change in porosity remains marginal. A micrographic documentation of both stones before and after treatment, taken at the same magnification, can be seen in Supplementary Data (Fig. S2).

As LdA has an inhomogeneous fabric, microscopic techniques are not reliable in confirming the presence of micro cracks. Therefore, sound speed propagation was measured before and after thermal treatment to confirm the presence of microstructural changes (Table 3). The ultrasound pulse velocity decrease after the thermal treatment, corresponding to longer traveling paths. This indicates widening of existing cracks and generation of new ones. Therefore, a reduction of soundness due to newly generated micro cracks was confirmed.

Phase transformation is likely to be initially limited to surface and subsurface layers as heat transfer proceeds from the outer parts to the inner core of the specimen and also because of the diffusion-limited escape of CO<sub>2</sub> resulting from carbonate decomposition. The mild thermal treatment adopted prevented decomposition or significant phase

**Table 1**

Color difference measured between pristine and thermally treated Apuan Marble (AM) and Lumaquela de Ajarte (LdA).

Stone	$\Delta L^*$	$\Delta a^*$	$\Delta b^*$	$\Delta E^*$
AM	9.17 ± 0.12	0.91 ± 0.03	2.31 ± 0.16	9.5 ± 0.11
LdA	-11.4 ± 0.57	0.58 ± 0.05	-2.53 ± 0.13	11.69 ± 0.58

$\Delta L^*$  the lightness coordinate ranging from 0 (black) to 100 (white), with negative values meaning darkening;  $\Delta a^*$  the red/green coordinate, with +a\* indicating redness and -a\* indicating greenness; and  $\Delta b^*$  the yellow/blue coordinate, with +b\* indicating yellowness and -b\* indicating blueness.

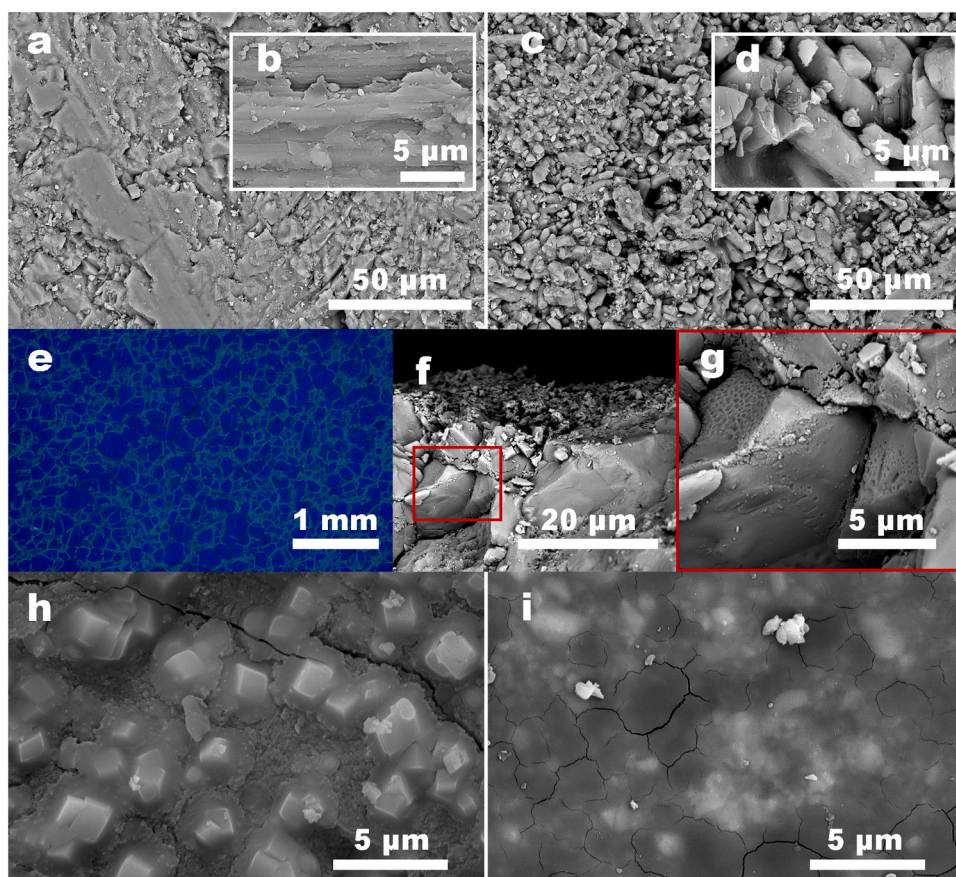


**Fig. 2.** Surfaces of freshly quarried a-b) Apuan Marble and c-d) Lumaquela de Ajarte displaying differing roughness as observed with a secondary electron detector. e) Inter- and intragranular microcracks in the fabric of Apuan Marble after thermal treatment. The visualization of cracks was performed using UV-light on a thin section embedded in a fluorescence resin. f-g) SEM images of a broken fragment of a thermally treated Apuan Marble sample showing f) precipitates on the surface, and g) a honeycomb-like texture, possibly as a result of beginning thermal degradation, located at an intergranular boundary in the vicinity of the surface. h) Backscatter electron images of embedded rhombohedral crystal in the nanosilica matrix on the surface of thermally treated Apuan Marble and, i) secondary electron images of the discoloration of the nanosilica matrix due to calcium mobilization on surfaces of thermally treated Lumaquela de Ajarte.

**Table 2**

Porometric data from mercury intrusion tests for specimens in pristine and thermally treated (aged) conditions for Apuan Marble and Lumaquela de Ajarte.

	Apuan marble		Lumaquela de Ajarte	
	Pristine	Aged	Pristine	Aged
Total pore surface [ $\text{m}^2 \text{g}^{-1}$ ]	0.14	0.23	3.03	3.77
Average pore diameter [ $\mu\text{m}$ ]	0.08	0.24	0.15	0.14
Hg-total porosity [%]	0.72	3.58	23.85	25.12

**Table 3**

Sound speed propagation before (pristine) and after thermal treatment (aged) on Apuan Marble (AM) and Lumaquela de Ajarte (LdA).

Stone	$\text{km s}^{-1}$	Pristine	Aged
AM	Mean	6.17	2.17
	Max/Min	6.28/6.09	2.36/1.85
LdA	Mean	3.22	2.6
	Max/Min	3.27/3.15	2.65/2.52

transformations of the bulk material. Locally high  $\text{CO}_2$  concentration in pores may also have hindered phase transformations in calcite [38]. On the surfaces, changes caused by thermal treatment were mostly observed in the form of small precipitates, as is the case for AM (Fig. 2f). Moreover, a honeycomb-like texture on the mineral is observed in the sub-surface area of the same carbonate, which might be an effect of the thermal treatment (Fig. 2g). Here, the vicinity to the surface and the newly opened cracks offer escape routes for  $\text{CO}_2$ , favoring the progress of thermally induced degradation processes.

The SEM analysis clearly indicates products of the thermal decomposition on the surface of AM, showing the presence of rhombohedral crystal bundles of  $\sim 1 \mu\text{m}$  cross-section (Fig. 2h). However, the solvent of

the silica sol may be a possible aid in the growth of well-formed crystal nuclei during re-carbonation. Future experiments with solvent and without silica should address this possibility. Moreover, a rim present in the silica matrix around the newly formed calcite crystals shows that calcium is mobilized, since a concentration gradient can be observed around the calcite crystals embedded in the silica matrix (see SEM/EDX spectra in Supporting Data Fig. S3a). Concerning LdA, phase transformation is only indicated by a whitish discoloration of the nanosilica consolidating matrix, which presents a distinguished intensity in Ca-Si ratio, as detected by SEM/EDX (Fig. S3b). Well-formed crystals are not observed for this carbonate under the given conditions. Therefore, changes on surfaces of AM are indicative to be more severe when compared to those present at surfaces of LdA. Overall, the post-treatment with colloidal nanosilica proved useful in preserving newly formed species embedded in the silica matrix.

### 3.2. Phase evolution with temperature as analyzed by in-situ XRD

In-situ XRD allowed us to follow the phase transformations from the onset a function of temperature. Fig. 3a and b illustrates the quantitative phase evolution with temperature obtained from Rietveld refinement of the XRD patterns (exemplary diffractograms can be seen in Figs. S4 and S5). The two samples follow the same trend of thermal decomposition and re-carbonation, but to different extents and with varying offsets concerning initial decomposition. For AM, the presence of CaO is first detected (approx. 1 wt%) after 10 min isothermal treatment at  $600^\circ\text{C}$  in the first heating cycle (see Fig. 3a). At the end of the three subsequent heat/cool cycles, the amount of newly formed CaO is 78.8 wt%, the remaining fraction being  $\text{CaCO}_3$ , which has decreased from its initial total amount of 98.8 wt%. The small fraction of dolomite disappears after the first heating cycle during the isothermal stage at  $600^\circ\text{C}$ . Accurate quantification of the products of dolomite decomposition into

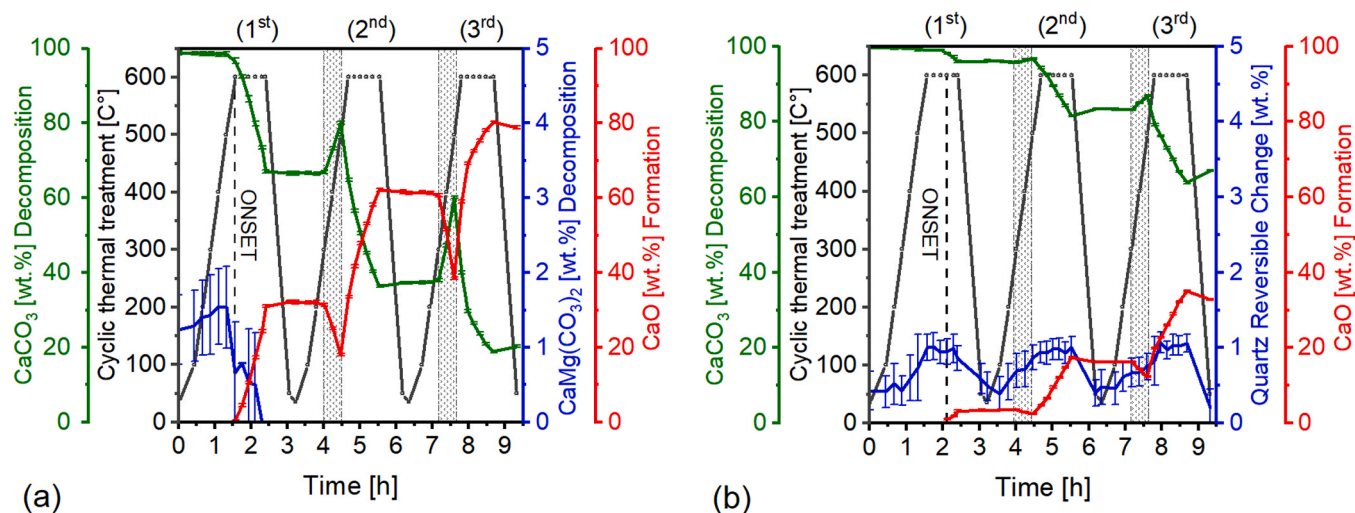


**Fig. 3.** Phase evolution (wt%) with temperature obtained from Rietveld refinement of in-situ XRD patterns for a) Apuan Marble and b) Lumaquela de Ajarte. Shaded areas highlight the retrograde reaction (in the second and third heating ramp) while the dotted line indicates the onset of thermal decomposition during the isothermal treatment (only reported for the first thermal cycle). (For interpretation of the references to colour in this figure legend, the reader is referred to the web version of this article.)

periclase or brucite was not possible because of their low abundances (< 2 wt%) and texture effects.

The onset of thermal decomposition for LdA is delayed compared to AM and occurs after 40 min of the first isothermal stage at 600 °C. At the end of the three heat/cool cycles, the absolute amount of newly formed CaO is ~32 wt%, and correspondingly the remaining calcium carbonate accounts for ~67 wt%. Quartz transforms reversibly from its room temperature form  $\alpha$ -quartz to  $\beta$ -quartz at 573 °C at one atmosphere of pressure. Due to its low amount (< 1 wt%), the fluctuations in phase fraction observed during the thermal cycles (Fig. 3b) are likely caused by the structural changes produced by the phase transition, as explained in [Supplementary Data, Fig. S6](#).

The difference in the onsets of thermal decomposition and the final conversion degrees for the two carbonates can be ascribed to their different microstructural features (i.e., sample surface roughness and porosity) exerting control on thermal transport properties [39]. As the thermal conductivity of air at 600 °C is lower than that of calcite, the former acts as an insulator, slowing down heat transfer more effectively in the porous variety of LdA compared to AM. Overall, the more densely packed AM decomposes earlier because the intergrain thermal resistance is low due to the higher surface area of contact between grains.

An intriguing observation on both carbonates is the retrograde reaction, through which the metastable CaO transforms back to CaCO<sub>3</sub> (Fig. 3, shaded areas). The high-temperature thermal decomposition  $\text{CaCO}_{3(s)} \rightarrow \text{CaO}_{(s)} + \text{CO}_{2(g)}$  is typically followed, under normal environmental conditions, by re-carbonation as a two-step reaction. This involves absorption of atmospheric H<sub>2</sub>O and results in the formation of a hydrated Ca(OH)<sub>2</sub> intermediate. Subsequent absorption of atmospheric CO<sub>2</sub> with release of H<sub>2</sub>O causes the net back reaction  $\text{CaO}_{(s)} + \text{CO}_{2(g)} \rightarrow \text{CaCO}_{3(s)}$ . While the presence of residual water can be excluded after the first thermal cycle, the highly reactive CaO is metastable also in the presence of CO<sub>2</sub> for the thermally treated specimens during the cooling and re-heating cycles, because some CO<sub>2</sub> is confined within their porous structures. The activation energy for the back reaction is provided by temperatures ranging from ~400 °C to ~500 °C, as shown by the reversal of the phase transformations in the last stage of the second and third heating ramps (shaded areas in Fig. 3). This structural reorganization (i.e., decomposition/re-carbonation reaction) and the cyclic heat-treatments are responsible for a surface limiting transformation, preserving the outer shape of the specimen, and allowing us to carry out streaming current and potential measurements.

### 3.3. Time-resolved monitoring of $\zeta$ and pore conductivity of pristine and thermally treated samples

By using the AGC configuration, the true  $\zeta$  values,  $\zeta\text{-True}(I_{\text{str}})$  and  $\zeta\text{-True}(U_{\text{str}})$ , are obtained (Fig. 4a–d). A key finding using the AGC is that  $\zeta$  values resulting solely from the carbonates surface exhibit differing electrokinetic potentials and drift directions for the two studied specimens. The dense variety AM starts at a  $\zeta\text{-True}$  of –19 mV and remains negative over 60 h of continuous measurements, reaching a nearly stable value of approximately –10 mV within the first 24 h (Fig. 4a and b). Conversely, LdA exhibits an initially positive  $\zeta$ -potential that shifts to negative values after ~30 min (Fig. 4c and d). Moreover, AM, the dense crystalline material with a rather smooth surface, under the studied conditions dissolves (or reacts) less and more slowly than LdA, which is an inhomogeneous, rough and brittle conglomerate. Therefore, one distinctive difference between pristine LdA and AM is that the former always causes larger pH shifts in contact with a neutral solution as it has a higher surface roughness. For macroscopic flat surfaces, the surface roughness, which comprises all textural and microstructural features of the stone surface including effects of grain edges and boundaries, is known to contribute to the reactivity of the carbonates as it is related not only to the specific surface area but also to varying crystal faces and defect density [40]. Similarly, for crystal surfaces, surface topography influences the reactivity of calcite [41]. For AM, the pH first increases and then decreases slightly. The decrease corresponds to a proceeding equilibration which is not reached in the given time-frame.  $\zeta$  becomes less negative with time, which can be attributed to dissolution. This can also be confirmed by a constant increase of the bulk conductivity. The results show that a lack of equilibrium is responsible for the differing  $\zeta$ -potentials in different carbonates. Besides, the specific surface area and the related reactivity of a given carbonate determines the delay time before a meaningful electrokinetic potential is reached within the initial periods of testing.

As concerns the pore conductivity of the stones in pristine conditions, its contribution affects the recorded streaming potential as a result of the presence of additional pathways for the conduction current through the porous network. By comparing the pore conductivity of pristine AM and LdA it is evident that porosity and pore conductivity correlate, a higher pore conductivity corresponding to a higher surface porosity. Thus, the higher the porosity, the more severe the underestimation of  $\zeta$  as determined by streaming potential (see the difference between  $\zeta\text{-I}_{\text{str}}$  and  $\zeta\text{-U}_{\text{str}}$  in Fig. 4). The pore conductivity causes an underestimation of  $\zeta\text{-U}_{\text{str}}$



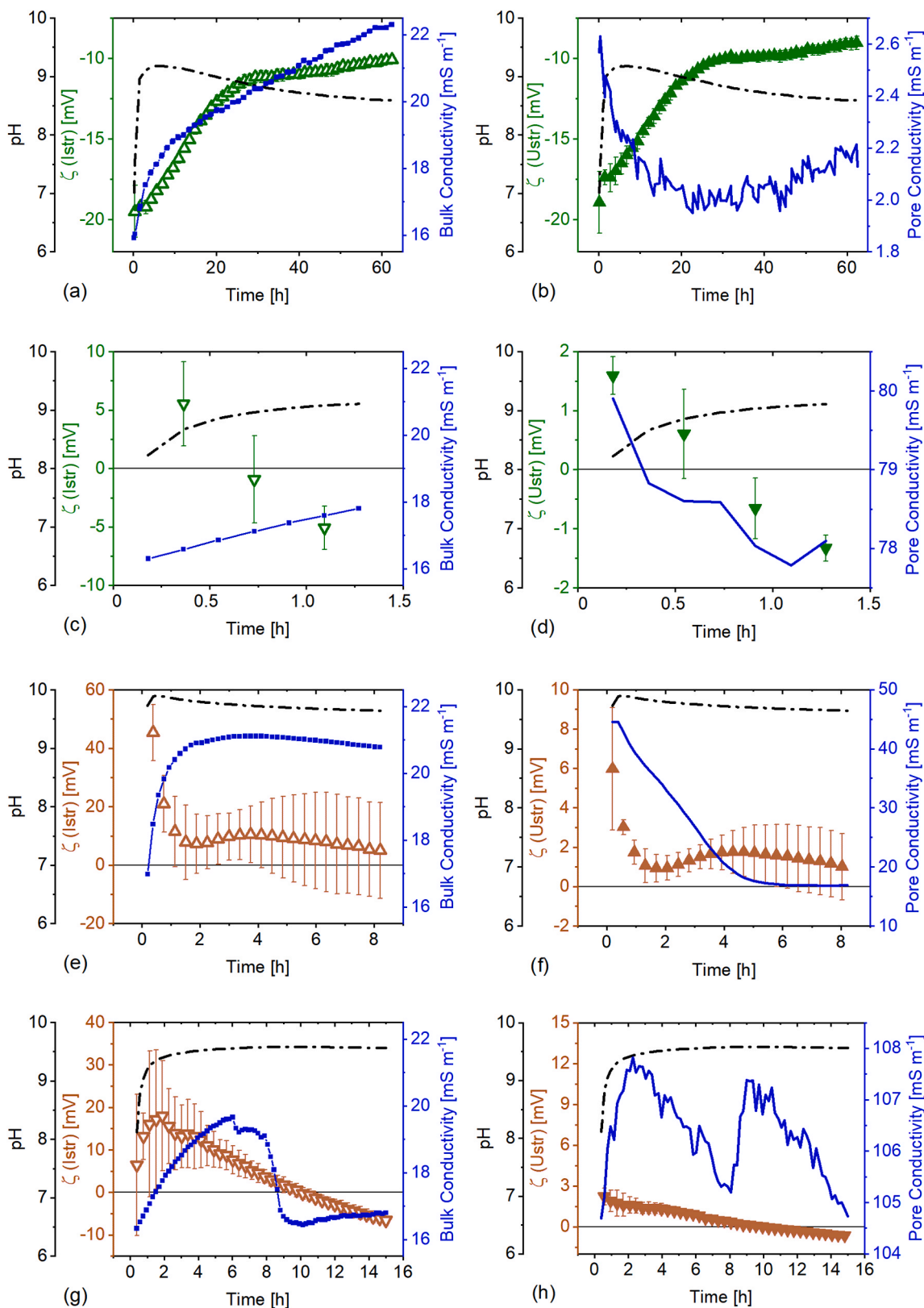


**Fig. 4.** Time evolution of  $\zeta$  as obtained from streaming current ( $I_{str}$ ) and streaming potential ( $U_{str}$ ) measurements with corresponding pH, bulk- and pore conductivity measurements, on pristine (green) and thermally treated (red) surfaces. Measurements performed with the AGC (pristine) and CC (thermally treated) configurations using an aqueous  $10^{-3}$  M KCl probing electrolyte solution: a-b) pristine Apuan Marble; c-d) pristine Lumaquela de Ajarte; e-f) thermally treated Apuan Marble ( $\zeta$ -Aged<sub>1.5</sub>) and g-h) thermally treated Lumaquela de Ajarte ( $\zeta$ -Aged<sub>1.5</sub>). Tests were performed until  $\zeta$  stabilizes or the isoelectric point ( $IEP_{pH}$ ) was approached/reached. (For interpretation of the references to colour in this figure legend, the reader is referred to the web version of this article.)

values by up to 90% in the case of the highly porous LdA, whereas the underestimation amounts to < 10% for pristine AM. After the thermal treatment, the underestimation of AM increases up to 80% while for LdA it remains the same due to its high porosity even in the pristine state.

The thermally treated samples ( $\zeta$ -Aged<sub>1.5</sub>) expose mixed calcite and calcium hydroxide surfaces. The positive  $\zeta$  measured for thermally treated samples may be explained by a combination of solubilization and re-adsorption processes involving calcium hydroxide, with preferential solubilization of the hydroxide anion along with preferential re-adsorption of solubilized  $\text{Ca}^{2+}$  cations. The slow decrease of the absolute value of  $\zeta$  and ultimately sign reversal from positive to negative might be the result of multiple processes that possibly change with time, involving also residual calcium oxide from underneath the hydroxide layer. Kinetic processes including physical and chemical adsorption as well as coupled dissolution-precipitation reactions might explain why  $\zeta$  is altered [42,43]. By comparing the pH and bulk conductivity evolution over time upon contacting the thermally treated specimens, it is indicative that the electrokinetic potential will depend on the amount of reactive material present at the surface. While neither the exact fractional amount of reactive phases nor the effective surface area are known, the results of the measurements performed with the CC (and thus involving the reference PP surfaces) clearly show that the phases that are more reactive govern the net electrokinetic potential (Fig. 4e–h). Thermally treated AM exhibits a higher pH increase and larger magnitude of  $\zeta$  during the initial period of the experiments as compared to LdA. This difference in alkalinity between the carbonates corresponds to the in-situ XRD analysis with AM having a higher amount of calcium oxide formed than LdA. This can be further confirmed by the increase of bulk conductivity in the initial period during the experiments and the absolute values (compare the steepness of the bulk conductivity curve between AM and LdA < 2 h and the absolute values reached). Likewise, the isoelectric point ( $\text{IEP}_{\text{pH}}$ ) will be influenced by the surface fraction of phase-transformed species (Table 4). After the initial period, the pH remains nearly constant for the thermally treated samples. The reactivity of calcite is indicated by alterations in  $\zeta$ , bulk- and pore conductivity. For AM-Aged<sub>1.5</sub>  $\zeta$  approaches zero after 8 h of testing. Changes in pore conductivity reflect solution changes in the micro-channel. The bulk conductivity decreases only slightly after 3 h of testing. Similarly,  $\zeta$  of LdA-Aged<sub>1.5</sub> approaches zero after 8 h. Unfortunately, the pore conductivity alterations on LdA surfaces cannot be tracked with great precision as the readings are suppressed by the presence of high surface porosity. The bulk conductivity of LdA starts decreasing after approx. 6 h of testing. Normally, a decrease on bulk conductivity indicates that ions are removed from the solution but more experiments are needed to confirm these alterations in regard to  $\zeta$  and to rule out experimental errors.

In general, the time-resolved measurements show that the carbonates are prone to partial dissolution, which is known to cause differences in  $\zeta$  [44,45]. Such processes are responsible for changes in composition of both the surface and the solution (pH and ionic strength), and therefore of the EDL instantaneous composition. Even if in conditions far-from-equilibrium, the dynamics of these surfaces can be followed through the induced alterations in  $\zeta$ , pH, bulk- and pore conductivity, which in turn allow to estimate time-dependent changes of these

systems. Thus, nonequilibrium phenomena or time dependent changes in  $\zeta$  allow to study effects of ageing, temperature or modifications of the composition of contacting solutions that are important for various applications [46–48].

### 3.4. pH-dependent electrokinetic measurements

When a reactive surface undergoes pH-dependent dissolution and reprecipitation reactions, the associated phenomena cause local perturbations in pH and ionic strength, which may extend to several molecular layers above the surface. In such cases, the possibility that the electrokinetic measurements do not accurately represent the electrokinetic charge and the occurring surface processes, has to be considered. On the other hand, while the absolute  $\zeta$  values from single-point measurements may be significantly affected by the nonequilibrium interfacial dynamics and the ensuing perturbations of the probing electrolyte solution,  $\text{IEP}_{\text{pH}}$  can be taken as a more reliable parameter; therefore, the electrical properties of the surfaces will be discussed based on this property, taken as a measure of the modifications occurring at the surface. The pH- and salinity dependent behavior of the carbonates was studied by performing a series of electrokinetic measurements over a defined pH range (hereafter referred to as titration), with the goal of analyzing the differences in surface reactivities of the two carbonates according to their different nature and as caused by the effects of thermal treatment and environmental re-carbonation processes.

In Fig. 5 it is evident that the thermal treatment had an effect on  $\zeta$  and the  $\text{IEP}_{\text{pH}}$  for AM as opposed to LdA. The effect on AM can be discussed in terms of an enhanced alkaline behavior after thermal treatment ( $\zeta$ -Aged<sub>24</sub>) and a recovery due to re-carbonation ( $\zeta$ -Aged<sub>365</sub>), while the measurements on LdA are not significantly affected by the thermal treatment due to its higher porosity promoting solubilization of the carbonate surface already before the thermal treatment. Specifically, the  $\zeta$ -Aged<sub>24</sub> results for AM can be explained by its chemical surface composition consisting of strongly alkaline CaO that quickly hydrates to  $\text{Ca}(\text{OH})_2$  upon contact with the electrolyte solution. This causes  $\zeta$  to remain positive throughout the whole explored pH range as a result of preferential solubilization of the hydroxide anion and/or increased preferential re-adsorption of  $\text{Ca}^{2+}$  cations (Fig. 5a), as already discussed in Section 3.3. By titrating from neutral towards increasingly alkaline pH,  $\zeta$ -Aged<sub>24</sub> decreases in magnitude and  $\text{IEP}_{\text{pH}}$  is eventually reached at  $\text{pH} \approx 11$ . Even one year after the thermal treatment, a complete recovery of the surface towards the original carbonate does not occur; this is shown by the shift in  $\text{IEP}_{\text{pH}}$  from pH 3.4 of the pristine stone to pH 4.6 for Aged<sub>365</sub>. The observed slight difference between  $\zeta$ -Pristine and  $\zeta$ -Aged<sub>365</sub> can be at least partially explained by a more effective release of lattice ions after thermal treatment and re-carbonation, ascribed to the increased specific surface area and enhanced solubility of the newly generated carbonate surfaces. Furthermore, the absence of organic matter contamination (completely removed, if initially present, by the thermal treatment) may further contribute to a less negative  $\zeta$  value in the Aged<sub>365</sub> sample [49]. In addition, AM Aged<sub>365</sub> samples displayed a cell resistance of  $\sim 450$  kOhm, much lower than the  $\sim 1150$  kOhm of the pristine sample (Table 5). The decrease in electrical resistance inside the streaming channel gives additional evidence for the thermally altered

**Table 4**

Summary of relevant properties of pristine and thermally treated (Aged<sub>1.5</sub>) Apuan Marble (AM) and Lumaquela de Ajarte (LdA) as determined in the asymmetric (CC) and the symmetric (AGC) cell configuration. Note that absolute values of pore conductivity can only be compared for same configurations and sample conditions, as both the cell resistance and the bulk conductivity depend on the amount of the sample tested and therefore, on the type of cell used.

Sample	$\zeta$ - <sub>str</sub> [mV]	Testing pH	$\text{IEP}_{\text{pH}}$	Cell Res. [kOhm]	Pore Cond. [mS/m]
AM (AGC) Pristine	$-19 \pm 1.6$ to $-10 \pm 0.3$	7–8.6	n/a	$623 \pm 53$	2.5–2.1
LdA (AGC) Pristine	$5.5 \pm 3.6$ to $-5.1 \pm 1.9$	8.2–9.1	8.9	$151 \pm 1$	78–77
AM (CC) Aged <sub>1.5</sub>	$45 \pm 9.5$ to $-5.0 \pm 1.6$	9.6–9.8	$\sim 9.8$	$170 \pm 28$	44–16
LdA (CC) Aged <sub>1.5</sub>	$18 \pm 13$ to $-6.5 \pm 1.3$	8.1–9.6	$\sim 9.6$	$139 \pm 2$	107–104

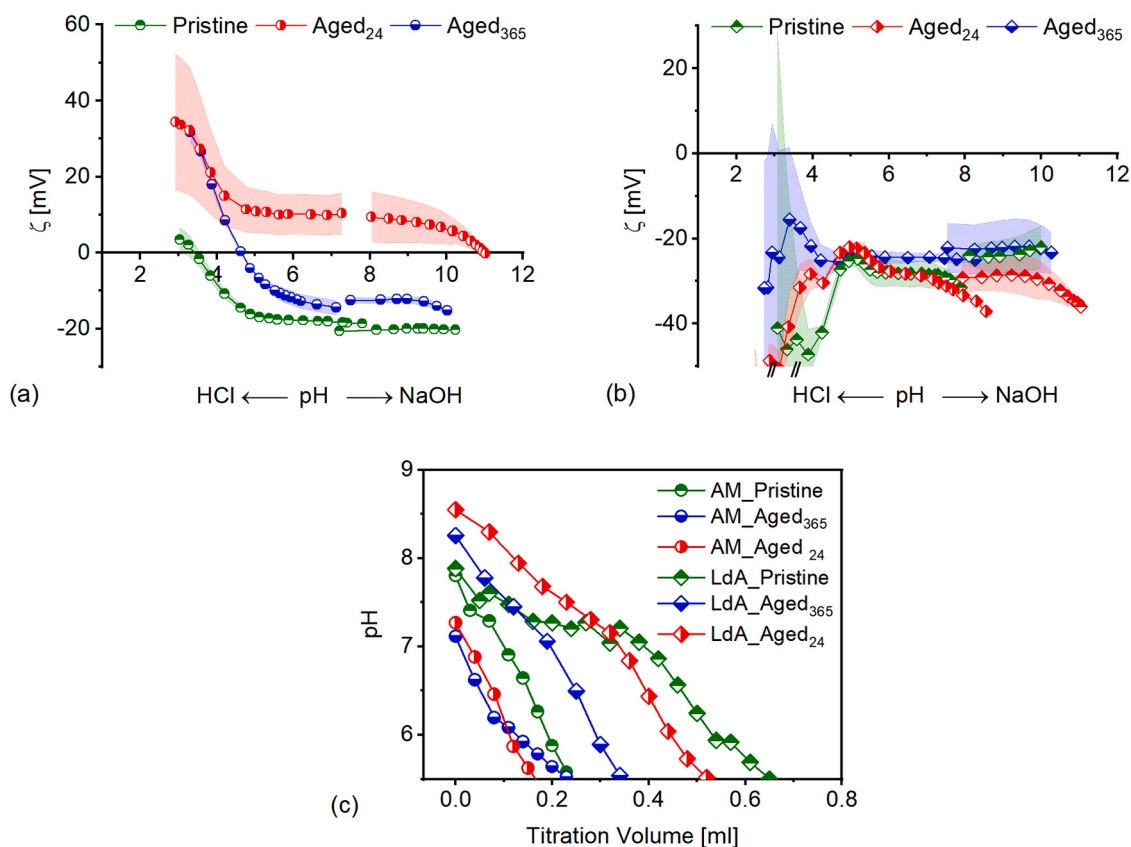


**Fig. 5.** Streaming current titration in the  $3 < \text{pH} < 11$  range performed on pristine and thermally treated (Aged<sub>24</sub>, Aged<sub>365</sub>) surfaces of a) Apuan Marble, and b) Lumaquela de Ajarte, as analyzed in CC configuration ( $\text{N}_2$ -purged  $10^{-3}$  M aqueous KCl probing solution). The shaded areas represent standard deviation ranges. Note that these results involve a combination of pH and salinity variations as the ionic strength changes during titration. Panel c) exhibits the initial pH after rinsing versus titration volume added to reach a pH of 5.5 for both stones and all studied conditions. The auto titrator proceeds by adding given amounts of 0.05 M HCl aqueous solution to the probing electrolyte, thus the small pH shifts recorded in certain pH ranges are indicative of the buffering capacity by the material surface.

**Table 5**

Summary of relevant properties of pristine and thermally treated (Aged<sub>24</sub>, Aged<sub>365</sub>) Apuan Marble (AM) and Lumaquela de Ajarte (LdA) measured in the asymmetric cell configuration (CC). pH-dependent electrokinetic measurements are performed for each sample over the  $3 < \text{pH} < 11$  range (titration). Note that the pore conductivity refers to the result of single-point measurements in nearly neutral conditions (i.e., before titration; see Fig. S7 in the Supplementary Data).

Sample	$\zeta$ -I <sub>str</sub> [mV]	Testing pH	IEP <sub>pH</sub>	Cell Res. [kOhm]	Pore Cond. [mS/m]
AM (CC) Pristine	$-25.3 \pm 4.5$	3–11	3.4	$1164 \pm 44$	n/a <sup>a</sup>
AM (CC) Aged <sub>24</sub>	$5.3 \pm 3.6$	3–11	11	$310 \pm 43$	32
AM (CC) Aged <sub>365</sub>	$-12.9 \pm 0.2$	3–11	4.6	$453 \pm 1$	14
LdA (CC) Pristine	$-23.4 \pm 1.7$	3–11	n/a	$88 \pm 7$	228
LdA (CC) Aged <sub>24</sub>	$-28.1 \pm 8.9$	3–11	n/a	$101 \pm 11$	181
LdA (CC) Aged <sub>365</sub>	$-23.4 \pm 0.9$	3–11	n/a	$102 \pm 0.4$	184

<sup>a</sup> In the range of experimental error  $-2 \text{ mS m}^{-1}$  (dependent on the correct determination of the cell constant).

surfaces being more prone to dissolution.

Unlike for AM,  $\zeta$  of LdA does not reach IEP<sub>pH</sub> in the explored pH range (Fig. 5b) with values ranging between  $-22 \text{ mV}$  and  $-30 \text{ mV}$  for  $4 < \text{pH} < 10$  for all specimen conditions. No effect on  $\zeta$  and the IEP<sub>pH</sub> are present on surfaces of LdA (Aged<sub>24</sub>), which can be explained by faster re-carbonation. However, the pristine and Aged<sub>24</sub> LdA show

enhanced surface reactivity compared to the Aged<sub>365</sub> sample. This can be seen through the small pH shifts recorded in certain pH ranges that are indicative of the buffering capacity by the material surface (Fig. 5c). This conclusion is further supported by comparing the results of the initial  $\zeta$  measurement for each sample (i.e., the first  $\zeta$  value recorded for each titration scan, towards acid and basic pH, respectively). The smaller dispersion of  $\Delta\zeta = 2 \text{ mV}$  for LdA (Aged<sub>365</sub>) as compared with  $\Delta\zeta = 5\text{--}8 \text{ mV}$  for pristine and LdA (Aged<sub>24</sub>) may indicate higher reactivities of the surfaces. The best repeatability in the case of LdA (Aged<sub>365</sub>) occurs, we think, by coincidence rather than by any specific behavior of LdA. Much better correlation between the  $\zeta$  from the pH scans is observed for AM, independent of its condition.

A peculiar evolution of  $\zeta$  in the course of titration is observed at  $\text{pH} < 5$  where negative  $\zeta$  increases in magnitude. For pristine and LdA (Aged<sub>24</sub>), the increase in negative  $\zeta$  starts below  $\text{pH} 4.5$  while the  $\zeta$  of LdA (Aged<sub>365</sub>) first increases and passes an apparent maximum at  $\text{pH} \sim 3.2$  before decreasing again. Other than the reproducibility of  $\zeta$  for subsequent streaming current measurements at the native pH of the aqueous KCl solution, which we attribute to the varying reactivity of LdA samples, we explain the behavior of  $\zeta$  at lower pH by the effect of specimen porosity on  $\zeta$  analysis. Porous materials soaked with aqueous solution become conductive. In the course of the experiment the effect of this ionic conductivity increases with sample porosity and thickness. Both, porosity and thickness are significant for LdA. While pore conductivity suppresses  $\zeta$  as obtained from streaming potential measurements [50], the contribution of streaming current inside pores, which is enabled by the conductive pathways through interconnected pores [51], to the measured streaming current becomes dominant. The uptake of the aqueous solution into the carbonate by capillary force leads to a partially

soaked cuboid, which prevents quantification of the streaming current through the (wetted) porous network. Changes in the wetting of pore structures between subsequent streaming current measurements may also contribute to the increased standard deviation indicated by the shaded areas in Figs. 5a and b. Overall, the titration results further highlight the influence of surface roughness when assessing the net electrokinetic potentials of macroscopic solid samples. It should be noted that when reactive and rough surfaces are present, the location of the slip plane and the effective surface area that contribute to the recorded streaming current/potential values become inherently more difficult to identify than for well-defined samples. Studies on roughness and corresponding pore solutions and on dynamic solid-liquid interfaces are rare in the literature. Very few studies [52,53] have called attention to this specific and elusive, albeit crucial, issue.

### 3.5. Asymmetric cell configuration

When electrokinetic measurements are performed using the CC, due to the asymmetric cell wall configuration, corrections are required to obtain true  $\zeta$  values. This is because the microchannel consists of two different materials, each one contributing with its net surface charge to the overall  $\zeta$ . In their first description of a similar configuration, Walker et al. [36] assumed equal contributions from the reference poly(methyl methacrylate) and sample surfaces. More recently, the importance of weighing differently the contributions of each surface in a heterogeneous arrangement has been demonstrated [54,55]. This is of particular relevance in the case of reactive and/or porous surfaces that might contribute more significantly to the overall measured electrokinetic parameters. However, differences involving surface roughness and porosity, as affected by actual surface area and pore conductivity, and other factors such as hydrophilicity may significantly affect the results of single-point measurements. Differences in  $IEP_{pH}$  are more reliable (i.e. less affected by factors other than the surface chemistry) in providing the fractional contribution of the materials to the overall determined  $\zeta$ . For this purpose, a nonporous PP was used as the reference material and AM as the tested surface because it is more inert than LdA and its higher compactness allows easier fabrication of the thin rectangular specimens required to fit the AGC. Fig. 6a displays streaming current titration curves to account for the influence of the reference surface.

When using Eq. (17) to analyze the fractional contribution of the studied material through the  $IEP_{pH}$ , the influence of the reference PP surface cannot be neglected, as its contribution to the overall  $\zeta$  amounts to a minimum of  $\lambda = 0.3$ , and up to  $\lambda = 0.5$  for the initial conditions (that is, before starting the titration) based on single point

**Table 6**

Influence of the reference polypropylene (PP) surface on the overall measured  $\zeta$  as analyzed with the AGC in titration experiments performed on pristine AM, on PP, and on the combination of PP and AM, respectively, in a  $10^{-3}$  M KCl solution by determining the isoelectric points ( $IEP_{pH}$ ), single point measurements ( $\zeta(I_{str})$ ) and the initial pH after rinsing for all three setups.

	PP+AM	PP	AM
$IEP_{pH}$	5.6	4.8	5.9
$\zeta(I_{str})$	-28 to -33	-50 to -55	-16 to -19
Initial pH	7.9	5.8	8.9

measurements (see Table 6). The reactivity of AM can be appreciated through the induced increase of pH, after the standard preliminary rinsing procedure. The pH increase is related to the overall amount of reactive surface present in the microchannel, which results in a drift from the native pH of the probing electrolyte to pH = 7.9 in the case of the mixed PP+AM cell surface, versus pH = 8.9 when both walls of the microchannel are made of AM.

In practice, the simplifying assumption of equal contributions from sample and reference surfaces might be applicable if the surface to be characterized is comparable to that of the reference polymer, i.e., a nonconductive and nonporous material with similar surface roughness and hydrophilicity. However, in the case of large differences between the two surfaces, as it is the case for the rough, porous (i.e., high surface area) and hydrophilic (i.e., with a different and more effective charge formation mechanism compared to a polymer-water interface) carbonate stones, pore conductivity and net release/capture of ionic species make the contribution from the stone surface to the overall  $\zeta$  dominant. Due to its higher reactivity and brittleness, LdA was not tested to account for the asymmetric cell configuration, but the same considerations about the higher hydrophilicity and surface roughness are expected to apply even more so for this stone.

The use of two different cell configurations involves additional issues when it comes to the interpretation of the measurements of  $\zeta$  and  $IEP_{pH}$ , especially in our case, in which non-equilibrium measurements of reactive surfaces are involved. In previous studies Preočanin et al. [56] found that the measured  $IEP_{pH}$  was unaffected by the cell type, while Bukšek et al. [57] found a dependency of the measured  $\zeta$  on the geometry of microchannels and the size of the tested surface, and Lützenkirchen et al. [58] observed that  $IEP_{pH}$  can be affected by the level of roughness. In our measurements the  $IEP_{pH}$  value for PP was found to be only slightly affected by the cell type (from pH = 4.6 to pH = 4.8, see Fig. 6b); such slight variation may be ascribed to sample preparation (see Supplementary Data for the preparation method) and experimental

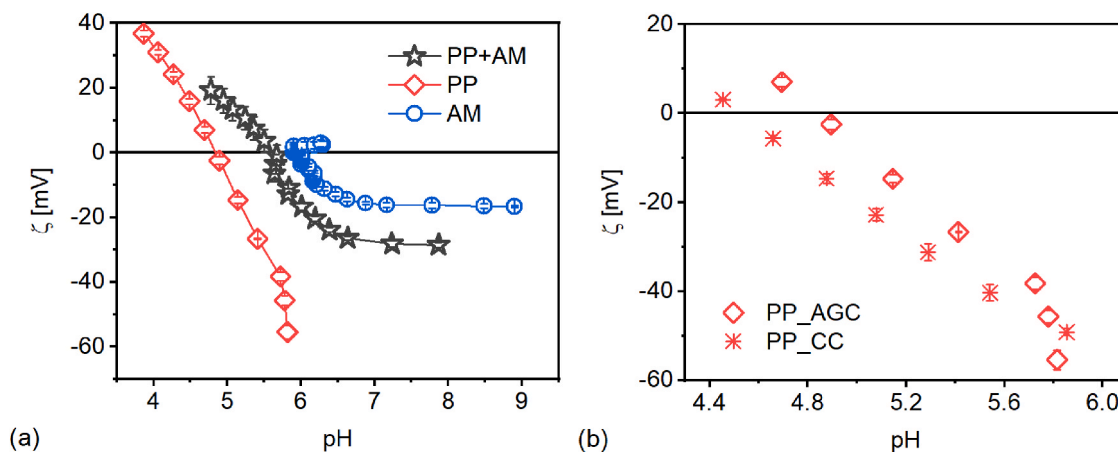


**Fig. 6.** a) Streaming current titration performed in the AGC on pristine Apuan Marble (AM), polypropylene (PP), and a combination of PP and AM to analyze the influence of the PP reference surface in an asymmetric cell configuration. b) Streaming current titration performed in the AGC and the CC on PP surfaces to analyze the influence of using two cell types. A nitrogen-purged  $10^{-3}$  M aqueous KCl probing solution was used. Note that these results involve a combination of pH and ionic strength variations as a result of both the titration of the probing electrolyte and of the pH-dependent solubility of the tested AM.

errors. However, when reactive materials are present, the surface area analyzed influences the solution chemistry and therefore the readings of  $\zeta$  and the IEP<sub>pH</sub>, which is why microchannel geometry takes on a governing role. For a more substantial discussion of the effect of the cell type on the electrokinetic measurements, more experiments are needed (e.g. to account for the possible effects of organic contaminants, instantaneous composition of the probing electrolyte solution, influence of lattice ions on the reference surface if any, etc.). Based on the obtained results, it is apparent that performing electrokinetic measurements with different cells does not lead to directly comparable quantitative data when reactive surfaces are involved. However, the topic of asymmetric cell arrangements, possibly with varying ratios of materials and differing roughness and/or porosities, remains relevant and understudied in light of mixed mineral surfaces that are common in nature. While the AGC is more appropriate for electrokinetic experiments, its limitation is the shaping of specimens to fit a microchannel; the use of the CC is thus justified for the purpose of comparing different surfaces and general trends.

#### 4. Conclusions

Streaming current and potential studies along with physical and chemo-mineralogical characterizations allowed us to follow surface alterations of two natural carbonates in pristine and thermally treated states. Their different reactivities under nonequilibrium conditions in the presence of dilute aqueous electrolytes was investigated. SEM analysis showed newly induced cracks on the thermally treated dense specimens of AM, while the same could not be observed on the inhomogeneous samples of LdA. However, porosimetry and sound speed propagation measurements indicated physical changes also in the fabric of LdA. SEM/EDX analysis showed embedded rhombohedral calcite crystals stabilized by a nanosilica coating applied onto the surface of AM after thermal treatment. For LdA a discoloration of the nanosilica coating occurred due to calcium mobilization. In-situ XRD confirmed that the thermal treatment results in different degradation extent and onset for the two stones. The dense stone AM decomposes earlier and has more calcium oxide on the surface than the porous stone LdA. In the initial period of time-resolved electrokinetic studies, the two analyzed carbonates in their pristine conditions exhibit distinctive electrokinetic potential drifts in opposite directions and differing  $\zeta$  signs. The initially negative  $\zeta$  value of AM shifts towards less negative values while the initially positive  $\zeta$  value of LdA change towards negative ones. Under nonequilibrium conditions, the sample surface roughness influences  $\zeta$ , as it contributes to dissolution. Thus, the larger effective surface area of LdA caused the strongest increase in solution pH, especially in the initial stages of the experiments. Pore conductivity was found to cause up to 90% underestimation of the absolute value of  $\zeta$  as assessed by streaming potential. Thermal treatment causes charge reversal from negative to positive for both stones as a result of calcium hydroxide solubility and the supply of Ca<sup>2+</sup> cations. Therefore, when mixed calcium hydroxide and calcite surfaces are present, the more reactive phases govern the net electrokinetic potential, even when their fractional surface coverage is low. Owing to the ability of these phases to affect conductivity and pH of the probing electrolyte solution, the amount of reactive phases also affect the IEP<sub>pH</sub>. The pH-dependent electrokinetic measurements further highlight the different behavior of the studied stones.  $\zeta$  of thermally treated AM is positive due to calcium hydroxide and a recovery of  $\zeta$  is evident due to re-carbonation. No such effect can be seen on LdA because it is porous and therefore re-carbonates faster and it more easily dissolves already in its pristine state. As a final remark, when due to experimental constraints an asymmetric cell configuration must be employed the fractional contribution of the reference polypropylene on the IEP<sub>pH</sub> must be considered. In our case the fractional contribution was found to amount to 0.3 and to the overall determined  $\zeta$  it can reach values of up to 0.5. The obtained data suggest that caution must be taken in the interpretation of results obtained from different cell

configurations in the case of reactive surfaces preventing reliable comparison of quantitative data.

#### Supplementary data

Permeability of the flow channel; chemical composition as measured by XRF; micrographs; porosimetric and density characteristics of AM; SEM-EDX analysis; exemplary XRD diffractograms and single-point streaming current and potential measurements.

#### Funding sources

M.B. is a doctoral candidate and acknowledges the support of the Marietta Blau Grant financed by the Austrian Federal Ministry of Education, Science and Research (BMBWF) and coordinated by the Austrian Agency for International Cooperation in Education and Research (OeAD). V.C. and S.B. acknowledge the support by "Nano-Cathedral", funded by the European Program Horizon 2020 Call NMP21-AC (GA 646178). A.V. acknowledges the support from the Czech Academy of Sciences (RVO 68378297). The authors acknowledge TU Wien Bibliothek for financial support through its Open Access Funding Programme.

#### CRediT authorship contribution statement

**Matea Ban:** Conceptualization, Investigation, Methodology, Data curation, Formal analysis, Funding acquisition, Validation, Visualization, Writing - original draft. **Thomas Luxbacher:** Validation, Formal analysis, Writing - review & editing. **Johannes Lützenkirchen:** Supervision, Resources, Writing - review & editing. **Alberto Viani:** Supervision, Resources, Writing - review & editing. **Sabrina Bianchi:** Supervision, Resources, Writing - review & editing. **Kludia Hradil:** Supervision, Resources, Writing - review & editing. **Andreas Rohatsch:** Investigation (petrographic description), Writing - review & editing. **Valter Castelvetro:** Conceptualization, Supervision, Resources, Writing - review & editing, Funding acquisition, Project administration.

#### Declaration of Competing Interest

The authors declare that they have no known competing financial interests or personal relationships that could have appeared to influence the work reported in this paper.

#### Acknowledgments

Werner Artner is acknowledged for his support in the X-Ray Centre of Vienna University of Technology and Milan Svoboda for the help with mercury intrusion porosimetry and He-pycnometry. Johannes Weber is recognized for his support in obtaining micrographs of thermally treated samples. The authors thank Colorobbia S.p.A for the supplied consolidant NC-12C. Paul Sonnleitner and Peter Urbanek are gratefully acknowledged for proofreading and generally supporting this work.

#### Appendix A. Supporting information

Supplementary data associated with this article can be found in the online version at [doi:10.1016/j.colsurfa.2021.126761](https://doi.org/10.1016/j.colsurfa.2021.126761).

#### References

- [1] G.E. Brown, How minerals react with water, *Science* 294 (2001) 67–69.
- [2] C.V. Putnis, E. Ruiz-Agudo, The mineral-water interface: where minerals react with the environment, *Elements* 9 (2013) 177–182.
- [3] P. Fenter, S. Kerisit, P. Raiteri, J.D. Gale, Is the calcite-water interface understood? Direct comparisons of molecular dynamics simulations with specular X-ray reflectivity data, *J. Phys. Chem. C* 117 (2013) 5028–5042.

- [4] D. Al Mahrouqi, J. Vinogradov, M.D. Jackson, Zeta potential of artificial and natural calcite in aqueous solution, *Adv. Colloid Interface Sci.* 240 (2017) 60–76.
- [5] S.L.S. Stipp, Toward a conceptual model of the calcite surface: hydration, hydrolysis, and surface potential, *Geochim. Cosmochim. Acta* 63 (1999) 3121–3131.
- [6] P. Moulin, H. Roques, Zeta potential measurement of calcium carbonate, *J. Colloid Interface Sci.* 261 (2003) 115–126.
- [7] A. Drechsler, A. Caspari, A. Synytska, Influence of roughness and capillary size on the zeta potential values obtained by streaming potential measurements, *Surf. Interface Anal.* 52 (2020) 991–995.
- [8] M. Elimelech, M. Nagai, C.-H. Ko, J.N. Ryan, Relative insignificance of mineral grain zeta potential to colloid transport in geochemically heterogeneous porous media, *Environ. Sci. Technol.* 34 (2000) 2143–2148.
- [9] M. Kosmulski, Isoelectric points and points of zero charge of metal (hydr)oxides: 50 years after Parks' review, *Adv. Colloid Interface Sci.* 238 (2016) 1–61.
- [10] L. Nachbaur, P.C. Nkinamubanzi, A. Nonat, J.C. Mutin, Electrokinetic properties which control the coagulation of silicate cement suspensions during early age hydration, *J. Colloid Interface Sci.* 202 (1998) 261–268.
- [11] A. Sanna, M. Uibu, G. Caramanna, R. Kuusik, M.M. Maroto-Valer, A review of mineral carbonation technologies to sequester CO<sub>2</sub>, *Chem. Soc. Rev.* 43 (2014) 8049–8080.
- [12] H. Manzano, R.J. Pellenq, F.J. Ulm, M.J. Buehler, A.C. van Duin, Hydration of calcium oxide surface predicted by reactive force field molecular dynamics, *Langmuir* 28 (2012) 4187–4197.
- [13] M. Gomez-Heras, S. McCabe, B.J. Smith, R. Fort, Impacts of Fire on Stone-Built Heritage, *J. Archit. Conserv.* 15 (2009) 47–58.
- [14] M. Garlock, I. Paya-Zaforteza, V. Kodur, L. Gu, Fire hazard in bridges: review, assessment and repair strategies, *Eng. Struct.* 35 (2012) 89–98.
- [15] Y. Praticò, J. Ochsendorf, S. Holzer, R.J. Flatt, Post-fire restoration of historic buildings and implications for Notre-Dame de Paris, *Nat. Mater.* 19 (2020) 817–820.
- [16] Jd.S. Vazzoler, G.L. Vieira, C.R. Teles, M.K. Degen, R.A. Teixeira, Investigation of the potential use of waste from ornamental stone processing after heat treatment for the production of cement-based paste, *Constr. Build. Mater.* 177 (2018) 314–321.
- [17] E. Martinho, M. Mendes, A. Dionisio, 3D imaging of P-waves velocity as a tool for evaluation of heat induced limestone decay, *Constr. Build. Mater.* 135 (2017) 119–128.
- [18] A. Ozguven, Y. Ozcelik, Effects of high temperature on physico-mechanical properties of Turkish natural building stones, *Eng. Geol.* 183 (2014) 127–136.
- [19] F. Vagnon, C. Colombero, F. Colombo, C. Comina, A.M. Ferrero, G. Mandrone, S. C. Vinciguerra, Effects of thermal treatment on physical and mechanical properties of Valderi Marble - NW Italy, *Int. J. Rock. Mech. Min. Sci.* 116 (2019) 75–86.
- [20] M. Prus, K. Szymanek, J. Mills, L.N. Lammers, W. Piasecki, K. Kedra-Krolik, P. Zarzycki, Electrophoretic and potentiometric signatures of multistage CaCO<sub>3</sub> nucleation, *J. Colloid Interface Sci.* 544 (2019) 249–256.
- [21] R.L. Folk, Practical petrographic classification of limestones, *AAPG Bull.* 43 (1959) 1–38.
- [22] R.J. Dunham, Classification of carbonate rocks according to depositional textures, in: W.E. Ham (Ed.), *Classification of Carbonate Rocks*, American Association of Petroleum Geologists Memoir, 1962, pp. 108–121.
- [23] CEN, Standard EN 14579: Natural stone test methods. Determination of Sound Speed Propagation, 2005.
- [24] CEN, Standard EN 15886, Conservation of cultural property. Colour Measurement of Surfaces, 2010.
- [25] T. Degen, M. Sadki, E. Bron, U. König, G. Nénert, The HighScore suite, *Powder Diff.* 29 (2014) S13–S18.
- [26] J. Faber, T. Fawcett, The powder diffraction file: present and future, *Acta Crystallogr. B Struct. Sci. Cryst. Eng. Mater.* 58 (2002) 325–332.
- [27] S.N. Kabekkodu, J. Faber, T. Fawcett, New Powder Diffraction File (PDF-4) in relational database format: advantages and data-mining capabilities, *Acta Crystallogr. B Struct. Sci. Cryst. Eng. Mater.* 58 (2002) 333–337.
- [28] A.A. Coelho, TOPAS and TOPAS-Academic: an optimization program integrating computer algebra and crystallographic objects written in C++, *J. Appl. Crystallogr.* 51 (2018) 210–218.
- [29] H.M. Rietveld, A profile refinement method for nuclear and magnetic structures, *J. Appl. Crystallogr.* 2 (1969) 65–71.
- [30] H. Bruus, *Theoretical Microfluidics*, Oxford University Press, Oxford, 2008.
- [31] C. Werner, H. Korber, R. Zimmermann, S. Dukhin, H.J. Jacobasch, Extended electrokinetic characterization of flat solid surfaces, *J. Colloid Interface Sci.* 208 (1998) 329–346.
- [32] D. Erickson, D. Li, C. Werner, An improved method of determining the zeta-potential and surface conductance, *J. Colloid Interface Sci.* 232 (2000) 186–197.
- [33] A. Cherubini, B. Garcia, A. Cerepi, A. Revil, Streaming potential coupling coefficient and transport properties of unsaturated carbonate rocks, *Vadose Zone J.* 17 (2018), 180030.
- [34] S. Li, P. Leroy, F. Heberling, N. Devau, D. Jougnot, C. Chiaberge, Influence of surface conductivity on the apparent zeta potential of calcite, *J. Colloid Interface Sci.* 468 (2016) 262–275.
- [35] F. Fairbrother, H. Mastin, CCCXII. Studies in electro-endosmosis. Part I, *J. Chem. Soc. Dalton Trans.* 125 (1924) 2319–2330.
- [36] S.L. Walker, S. Bhattacharjee, E.M. Hoek, M. Elimelech, A novel asymmetric clamping cell for measuring streaming potential of flat surfaces, *Langmuir* 18 (2002) 2193–2198.
- [37] S. Siegesmund, K. Ullemeyer, T. Weiss, E.K. Tschegg, Physical weathering of marbles caused by anisotropic thermal expansion, *Int. J. Earth Sci.* 89 (2000) 170–182.
- [38] B.R. Stanmore, P. Pilot, Review-calcination and carbonation of limestone during thermal cycling for CO<sub>2</sub> sequestration, *Fuel Proc. Technol.* 86 (2005) 1707–1743.
- [39] J.D. Merriman, A.M. Hofmeister, D.J. Roy, A.G. Whittington, Temperature-dependent thermal transport properties of carbonate minerals and rocks, *Geosphere* 14 (2018) 1961–1987.
- [40] C. Fischer, R.S. Arvidson, A. Lüttge, How predictable are dissolution rates of crystalline material? *Geochim. Cosmochim. Acta* 98 (2012) 177–185.
- [41] J. Colombani, The alkaline dissolution rate of calcite, *J. Phys. Chem. Lett.* 7 (2016) 2376–2380.
- [42] F. Heberling, T.P. Trainor, J. Lutzenkirchen, P. Eng, M.A. Denecke, D. Bosbach, Structure and reactivity of the calcite-water interface, *J. Colloid Interface Sci.* 354 (2011) 843–857.
- [43] F. Renard, A. Røyne, C.V. Putnis, Timescales of interface-coupled dissolution-precipitation reactions on carbonates, *Geosci. Front.* 10 (2019) 17–27.
- [44] I. Sondi, J. Bišćan, N. Vdović, S.D. Škapin, The electrokinetic properties of carbonates in aqueous media revisited, *Colloids Surf. A Physicochem. Eng. Asp.* 342 (2009) 84–91.
- [45] A. Hiorth, L.M. Cathles, M.V. Madland, The impact of pore water chemistry on carbonate surface charge and oil wettability, *Transp. Porous Med.* 85 (2010) 1–21.
- [46] E. Chibowski, L. Hotysz, A. Szcześ, Time dependent changes in zeta potential of freshly precipitated calcium carbonate, *Colloids Surf. A Physicochem. Eng. Asp.* 222 (2003) 41–54.
- [47] T. Liberto, C. Barentin, J. Colombani, A. Costa, D. Gardini, M. Bellotto, M. Le Merrer, Simple ions control the elasticity of calcite gels via interparticle forces, *J. Colloid Interface Sci.* 553 (2019) 280–288.
- [48] M.D. Jackson, J. Vinogradov, Impact of wettability on laboratory measurements of streaming potential in carbonates, *Colloids Surf. A Physicochem. Eng. Asp.* 393 (2012) 86–95.
- [49] L. Madsen, Calcite: surface charge. *Encyclopedia of Surface and Colloid Science*, CRC Press, 2015, pp. 801–813.
- [50] A. Yaroshchuk, V. Ribitsch, Role of channel wall conductance in the determination of  $\zeta$ -potential from electrokinetic measurements, *Langmuir* 18 (2002) 2036–2038.
- [51] A. Yaroshchuk, T. Luxbacher, Interpretation of electrokinetic measurements with porous films: role of electric conductance and streaming current within porous structure, *Langmuir* 26 (2010) 10882–10889.
- [52] M. Zembala, Electrokinetics of heterogeneous interfaces, *Adv. Colloid Interface Sci.* 112 (2004) 59–92.
- [53] A.E. Malevich, V.V. Mityushev, P.M. Adler, Electrokinetic phenomena in wavy channels, *J. Colloid Interface Sci.* 345 (2010) 72–87.
- [54] S. Laumann, V. Micic, G.V. Lowry, T. Hofmann, Carbonate minerals in porous media decrease mobility of polyacrylic acid modified zero-valent iron nanoparticles used for groundwater remediation, *Environ. Pollut.* 179 (2013) 53–60.
- [55] I. Petrić, H. Bukšek, T. Luxbacher, T. Pušić, S. Bischof, Influence of the structure of polymer fiber composites on the analysis of the zeta potential, *J. Appl. Polym. Sci.* 135 (2018) 46227.
- [56] T. Preočanin, A. Selmani, P. Lindqvist-Reis, F. Heberling, N. Kallay, J. Lützenkirchen, Surface charge at Teflon/aqueous solution of potassium chloride interfaces, *Colloids Surf. A Physicochem. Eng. Asp.* 412 (2012) 120–128.
- [57] H. Bukšek, T. Luxbacher, I. Petrić, Zeta potential determination of polymeric materials using two differently designed measuring cells of an electrokinetic analyzer, *Acta Chim. Slov.* 57 (2010) 700–706.
- [58] J. Lützenkirchen, G.V. Franks, M. Plaschke, R. Zimmermann, F. Heberling, A. Abdelmonem, G.K. Darbha, D. Schild, A. Filby, P. Eng, J.G. Catalano, J. Rosenqvist, T. Preočanin, T. Aytug, D. Zhang, Y. Gan, B. Braunschweig, The surface chemistry of sapphire-c: a literature review and a study on various factors influencing its IEP, *Adv. Colloid Interface Sci.* 251 (2018) 1–25.